

Integration of Dynamic Multi-Atlas and Deep Learning Techniques to Improve Segmentation of the Prostate in MR Images

Hamid Moradi* and Amir Hossein Foruzan[†]

*Department of Biomedical Engineering, Engineering Faculty
Shahed University, Tehran, Iran*

**h.moradi@shahed.ac.ir*

†a.foruzan@shahed.ac.ir

Received 7 November 2020

Accepted 29 April 2021

Published 14 July 2021

Accurate delineation of the prostate in MR images is an essential step for treatment planning and volume estimation of the organ. Prostate segmentation is a challenging task due to its variable size and shape. Moreover, neighboring tissues have a low-contrast with the prostate. We propose a robust and precise automatic algorithm to define the prostate's boundaries in MR images in this paper. First, we find the prostate's ROI by a deep neural network and decrease the input image's size. Next, a dynamic multi-atlas-based approach obtains the initial segmentation of the prostate. A watershed algorithm improves the initial segmentation at the next stage. Finally, an SSM algorithm keeps the result in the domain of allowable prostate shapes. The quantitative evaluation of 74 prostate volumes demonstrated that the proposed method yields a mean Dice coefficient of 0.83 ± 0.05 . In comparison with recent researches, our algorithm is robust against shape and size variations.

Keywords: Prostate segmentation; deep learning; watershed segmentation; probabilistic atlas; statistical shape modeling.

1. Introduction

Prostate disorders such as benign prostate hyperplasia (BPH), prostatitis, and prostate cancer, are common illnesses in men.¹ After Lung cancer, prostate tumors are the second most usual malignancy and the fifth cause of death in the male population. Moreover, the number of cases will reach 2.2 million by 2040.² Early diagnosis and treatment of the disease lead to the decline of the death rate. The main procedures for prostate cancer diagnosis are palpation, a blood test for measuring the prostate-specific antigen (PSA) level, and Trans-rectal Prostatic Ultrasound (TRUS).³ However, the treatment process depends on the tumor's stage, PSA level, Gleason score, and patient's age.⁴

[†] Corresponding author.

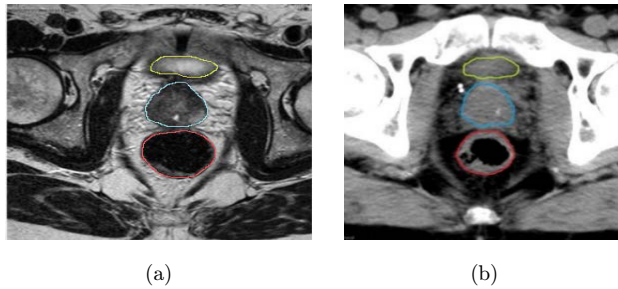


Fig. 1. (Color online) Prostate and nearby regions are shown in (a) MR and (b) CT images. Prostate, Rectum, and Bladder are shown in blue, red, and yellow, respectively.

Imaging techniques including ultrasonography, Computed-Tomography (CT)-Scan, and Magnetic Resonance Imaging (MRI) visualize the organ and estimate its shape and volume. These measurements are essential in diagnosis, radiotherapy planning, and treatment procedures.^{5,6} T2-weighted MR modality is the preferred imaging technique since it does not contain ionizing radiation. However, the appearance of the image depends on the acquisition protocol, field strength, coil profile, and scanner type.⁷ Figure 1 shows typical prostate regions in MR and CT images.

Manual segmentation of the prostate by an expert radiologist is a challenging, subjective, and time-consuming task. However, intensity inhomogeneity inside the prostate's region, imaging artifacts, and variations in the prostate's shape and size are significant challenges in automatic prostate delineation algorithms (Fig. 2).⁸

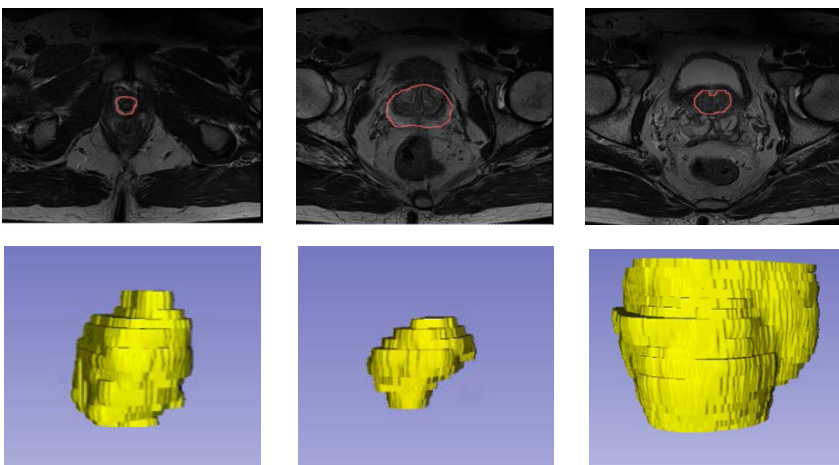


Fig. 2. (Color online) The top row depicts low contrast between the prostate (red contour) and its neighboring tissues in a typical MR image (Case 15). The bottom row represents high variation in the prostate's shape and size.

Here, we propose a hybrid method containing a deep neural network, the multi-atlas technique, and the Statistical Shape Modeling (SSM) to segment the prostate. Our innovations include the following:

- Defining the organ’s ROI by a Deep Neural Network (DNN) by integrating appearance and spatial features.
- Eliminating user-interaction and developing an automatic segmentation approach by a dynamic multi-atlas scheme.
- Improving the results in the base and apex regions by the watershed algorithm.

2. Previous Works

Main prostate segmentation methods include deep neural networks, Active Appearance/Shape Models (AAMs/ASMs), probabilistic atlases, and level sets.

Some hybrid methods take advantage of the methods mentioned above to enhance the performance of the algorithms. The privilege of the hybrid approaches is robust performance against imaging artifacts and noise.⁹ Other approaches are graph-cuts, decision forests, and watersheds. All these methods share common pre-processing steps including, Region of Interest (ROI) definition, image quality enhancement, and noise reduction. Interactive methods employed user interaction to delineate the prostate boundary in different slices. The RUNMC team proposed an interactive segmentation method that acquired a 0.80 mean Dice value.¹⁰

Deep learning is a recent development in neural networks, and it has obtained significant achievements in object segmentation. Deep learning is a recent development in neural networks, and it has obtained significant achievements in object segmentation. Guo *et al.* enhanced the Multi-Atlas Segmentation (MAS) technique by stacked autoencoder features; instead of handcrafted attributes. Therefore, they coped with variations of the organ’s appearance and MR images’ inhomogeneity. Finally, they refined their results by deformable models.¹¹

Latent features reduce the similarity between a landmark in the test image and irrelevant points in the training images and improve the correspondence between test and train data. Nelson *et al.*¹² and Rusu *et al.*¹⁰ presented automatic atlas-based methods for prostate segmentation with a result of 0.79 and 0.82 using the Dice index, respectively.

Karimi *et al.*¹³ extracted the 2D boundary of the prostate and prepared a point cloud. Then, they behaved the point cloud like an SSM. Their deep neural network estimates the positions of the point cloud for a test dataset. They regularized their network by spectral dropout and the Elastic net and increased the average Dice score from 0.80 to 0.88. Variations of deep networks are *Z*-net,¹⁴ Dense *U*-net,¹⁵ volumetric ConvNet,¹⁶ holistically nested network,¹⁷ and cascaded *U*-nets.¹⁸ Bredell *et al.*¹⁹ presented an interactive training strategy for CNNs with the capability and obtained a 0.97 Dice score.

Some researchers used a conventional AAM technique to segment the prostate in MR images.²⁰ Others improved the results by including a preprocessing step²¹ or employing textural information.²² However, their results are not good in the apex and base regions. Landmark selection and establishing a correspondence between these points are other issues in AAM/ASM-based approaches.²³ Mesadi *et al.*²⁴ used local appearance learning to improve their results in central and peripheral regions. They achieved a 0.83 Dice index.

Regarding atlas-based approaches, researchers used either a single probabilistic atlas (PA) or a set of template segmentations in the case of the multi-atlas technique. Then, they utilized different merging methods to aggregate the templates. Makni *et al.*²⁵ grouped similar training images and made more than one atlas to improve segmentation results. They employed the corresponding atlases to prepare an initial segmentation and later refined the outcome by an ASM deformable model. Litjens *et al.*²⁶ integrated the output of individual probabilistic atlases using the majority voting technique. Atlas-based approaches failed since the input MR image was substantially different from the training set. Variations of the prostate's shape and size and nonstandard intensity of MR images made the segmentation task challenging.²⁷ The performance of these methods was not acceptable in the apex region as well.

Level set approaches steer an initial contour towards an object's boundary using region or edge information. Region-based techniques obtain better since there is unreliable edge information in CT and MR images. Ghose *et al.*⁸ delineated the prostate's boundary using the random forest and later improved their results by region-based level set. They used individual decision forests for the apex, central, and base regions. Their method was computationally efficient, but its performance depended on the employed features used.

The structure of this paper is as follows. Details of the proposed method are in Sec. 3. We give the results and discuss them in Sec. 4 and conclude them in Sec. 5.

3. The Proposed Method

The framework of the proposed prostate segmentation method is shown in Fig. 3. We employ a set of manually segmented MR images as prior knowledge (a) to train a DNN, (b) to prepare a probabilistic atlas, and (c) to build an SSM model. The proposed method has five significant steps: (1) preprocessing, (2) ROI delineation using a DNN, (3) multi-atlas-based initial segmentation, (4) improvement of the result by the watershed algorithm, and (5) final refinement. Compared to our previous research,²⁸ we employed the watershed and modified the SSM algorithm, which improved some cases with inappropriate outcomes. For example, the Dice metric was boosted from 65.5% to 83.6% for case #7. In this research, we focused on improving the segmentation in the base and apex regions.

In the preprocessing, we compensated for the large misalignment of input images and enhanced their quality. A DNN determines the prostate's ROI to reduce the

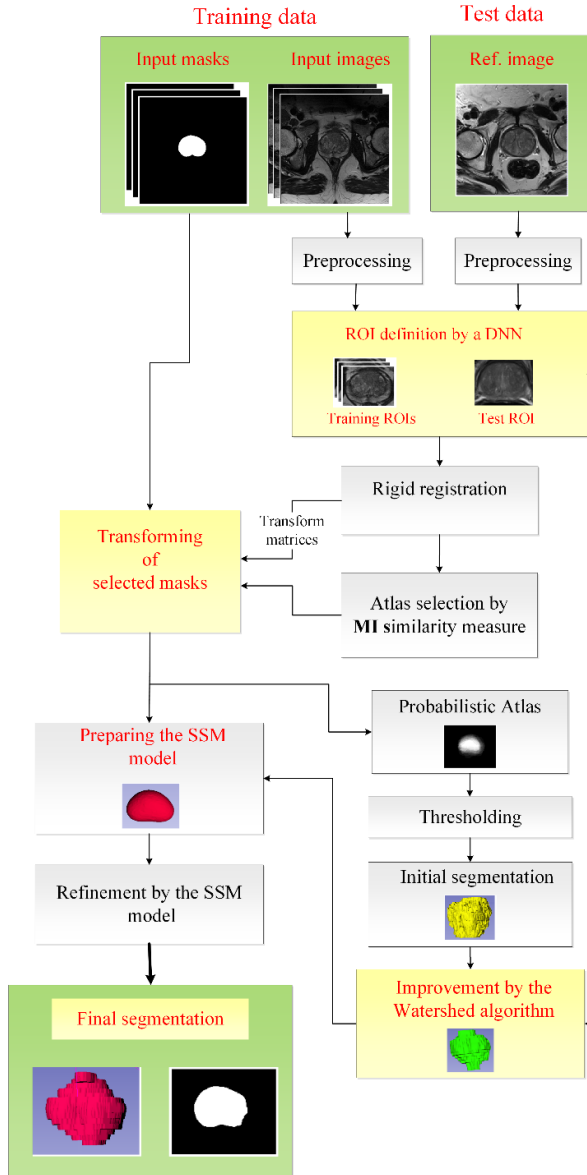


Fig. 3. The framework of the proposed prostate segmentation method.

image's size and decrease the false positive rate. Next, a multi-atlas segmentation technique integrated by an atlas selection process obtains the initial segmentation. We improve the initial outcome at the base and apex regions by the watershed algorithm. Finally, an SSM model refines the shape of the segmented prostate into the allowable shape domain.

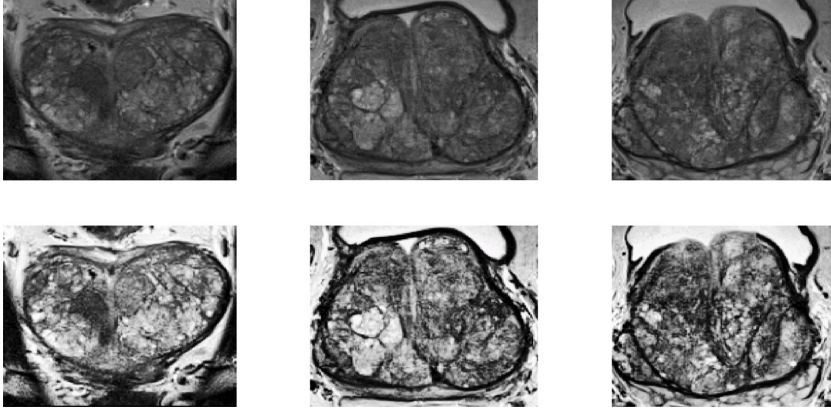


Fig. 4. Typical slices of input data (top row) and histogram equalized results (bottom row) are shown.

3.1. Preprocessing

An input MR image is frequently affected by imaging artifacts such as bias fields and noise. Moreover, data obtained from different scanners have various spacings, orientations, and origins. The preprocessing are (1) image’s origin, orientation, and spacing matching, (2) contrast enhancement, and (3) noise reduction. This step prevents the registration algorithm from trapping into local minimums.

We enhance image details and contrast by histogram equalization. Figure 4 shows typical slices of the input data before and after contrast enhancement. The Anisotropic Diffusion (AD) filter then reduces noise levels and preserve edges simultaneously that is crucial to the watershed algorithm.

3.2. ROI detection using a deep neural network

A deep neural network defines the ROI of the tissue in each slice. The employed features are both textural and spatial information. The feature vector contains intensities of 5×5 neighbors together with the (x, y) position of the corresponding pixel. Since the intensity of the tissue is similar to the neighboring organs, the output of the DNN contains nonprostate voxels. Incorporating spatial features improve the results, and it is a novelty in the proposed method.

The DNN model is a 10-layer network consisting of $27 \times 200 \times 300 \times 150 \times 100 \times 70 \times 20 \times 10 \times 5 \times 1$ neurons. The input data is a 1×27 feature vector, and the output is the label of the pixel. A validation set defined the hyper-parameters. The input dataset included 24 MR images. The numbers of training, validation, and test data were 16, 3, and 5, respectively. A Normal distribution initialized the weights of the network. The neurons’ activation functions were “Rectified Linear Units” (Relies), and the loss function of the optimization was the Adam algorithm. We refined the DNN’s outcome by morphological filters and set the

remaining pixels' bounding box as the prostate's ROI. The obtained area is expanded by five pixels from each side to ensure that the selected ROI covers all the prostate's pixels.

3.3. Initial segmentation by a dynamic multi-atlas technique

Another novelty in the proposed algorithm is employing a dynamic multi-atlas scheme to prepare the prostate's initial segmentation. Multi-atlas segmentation (MAS) is a recent technique in the segmentation of medical images. It considers each of the training data as an individual atlas and registers it to the input image. The corresponding transform matrix then warps the training masks that build a probability map.

We suggest a dynamic MAS approach to consider variations in the shape and size of the prostate. In a dynamic MAS, the atlas is prepared individually for each input image. Since the gland's size is proportional to the body mass index,²⁹ a dynamic atlas is more appropriate than a static atlas. We compare the test image with the training set using the mutual information (MI) measure. Then, the top 30% of similar training data are employed in the atlas preparation. Therefore, the probabilistic atlas varies with the input image, and we call this approach the dynamic multi-atlas technique. Details of the dynamic MAS are in the following paragraph (Fig. 5).

In conventional probabilistic atlases, an arbitrary training image is chosen as the reference, and the remaining training data are registered onto it.³⁰ This approach makes a bias toward the reference image. The bias effect decreases when the input image is the reference data. Therefore, we register the training images' ROI to the test data and select the top similar samples as the matched images. We then use the matched transform matrices for the registration of the training masks. The registered mask images are accumulated and thresholded to make the prostate's initial segmentation (Fig. 6).

We normalize the atlas before thresholding and use the Majority Voting (MV) approach to find the prostate's initial segmentation.

3.4. Improvement of the results by the watershed algorithm

We utilize the watershed algorithm to resolve the under-segmentation problem in the apex and base regions. Based on our experience, the prostate's boundary in the apex and base regions are delineated in the coronal and sagittal views better than the axial view. Therefore, the organ's initial boundary is eroded and used as the seed for a marker-based watershed algorithm. The prostate's background is defined by the dilation of the initial result. The optimum size of the erosion and dilation elements are 4 and 2 pixels, respectively. Figure 8 shows the application of the watershed algorithm on different views.

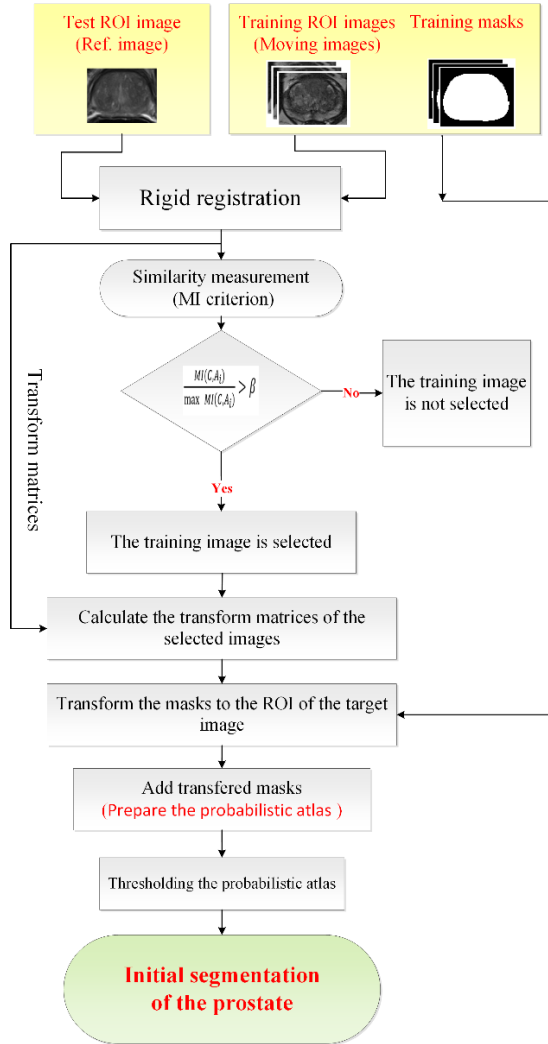


Fig. 5. The pipeline of the dynamic multi-atlas.

3.5. Final refinement

We assume that the prostate’s shape in the target image is similar to those of the training images. Therefore, we utilize a statistical shape model (SSM) to retain the prostate’s shape in the allowable Shape Domain. The training data of the dynamic multi-atlas build the shape model as well. Figure 7 illustrates the framework of the SSM method. A crucial step in an SSM is to find corresponding points. Based on previous experience, the Coherent Point Drift (CPD) algorithm is used, which is a robust algorithm. Details of the SSM are in Ref. 31.

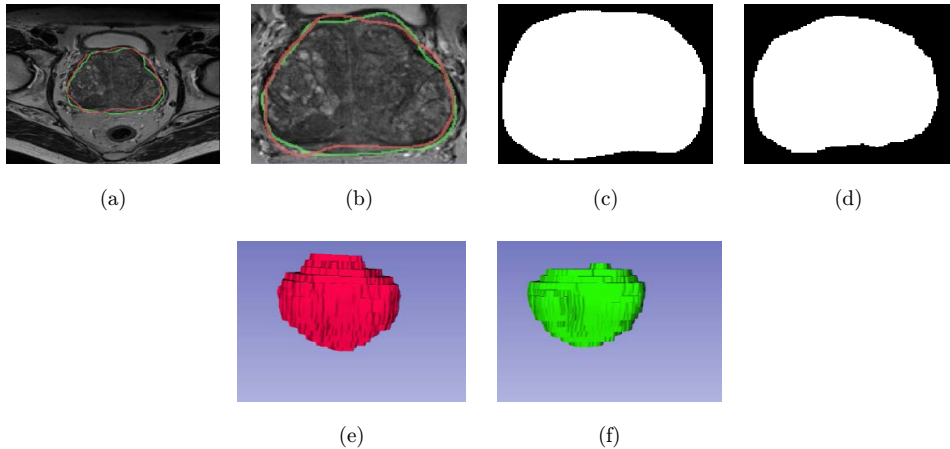


Fig. 6. Initial segmentation of Case #17. (a) Input MR image. (b) Prostate ROI. (c) The probabilistic atlas. (d) Initial segmentation. (e) Surface rendering of the initial segmentation and (f) the ground truth. Red and green contours indicate the proposed and ground_truth results.

4. Results and Discussions

4.1. Dataset

We evaluated our method using 24 NCI-ISBI 2013¹⁰ and 50 PROMISE-12⁷ transverse T2-weighted MR images. Table 1 demonstrates details of data acquisition protocols.

The hardware platform for the DNN code was an Intel® Core™ i7-6700K, 32 GB DRAM using an NVIDIA GeForce GTX1080 GPU with 16 GB DRAM. We implemented the code using Python on 64-bits MS-Windows. The remaining parts of the algorithm were coded in C++ and MATLAB environments on an Intel Core™ i7-4702MQ CPU @ 2.2 GHZ with 8 GB-DRAM running 64-bits Microsoft Windows. We used ITK-SNAP and 3D Slicer software to visualize the results.

4.2. Quantitative evaluation

We used several metrics including, Dice (DSC), Jaccard, Accuracy (ACC), and Error_Rate metrics (Table 2).

Table 1. Details of data acquisition protocols.

Dataset	Image num.	Field strength (T)	Endorectal coil	Resolution (in-plane/through-plane in mm)	Dimensions
PROMISE 12	50	1.5–3.0	Yes	0.27–0.75/2.8–4.0	256 * 256 * 18–23 512 * 512 * 23–54 320 * 320 * 15–24 384 * 384 * 28
NCLISBI 2013	24	3.0	No	0.27/2.2	320 * 320 * 15 – 24

Table 2. Mathematical definitions of the evaluation metrics.

Definition	Metric
A: Automatic segmentation	$\text{DSC} = \frac{2 A \cap M }{ A + M }$ $\text{Jaccard} = \frac{ A \cap M }{ A \cup M }$ $\text{Accuracy} = \frac{\text{TP} + \text{TN}}{\text{TP} + \text{TN} + \text{FN} + \text{FP}}$ $\text{Error Rate} = \frac{\text{FP} + \text{FN}}{\text{TP} + \text{TN} + \text{FN} + \text{FP}}$
M: Manual segmentation	
True Positive (TP): $ A \cap M $	
False Positive (FP): $ A \cap M^C $	
True Negative (TN): $ A^C \cap M^C $	
False Negative (FN): $ A^C \cap M $	

Note: The complements of A and M are shown by A^C and M^C , respectively.

The proposed algorithm’s outputs in different stages are in Table 3. These steps are Dynamic multi-atlas (DMA), refinement by the watershed technique (DMA + Watershed), and final improvement by the SSM (DMA + Watershed + SSM). As is shown in Table 3, each step improves the results individually.

We classify the dataset into images with severe/minor intensity inhomogeneity. The first group’s results are 0.10 lower than the normals. Concerning the data with minor intensity inhomogeneity, average Dice and Jaccard indices are 0.85 and 0.73, respectively. Table 4 is a comparison between our method with recent researches in MR prostate segmentation methods.

Concerning Table 4, some of the data used by Guo *et al.* were enhanced by endorectal coils. Similar to the method of Karimi,¹³ we integrated deep learning and SSM; moreover, we used nonrigid CPD to build the SSM. DNN removes false positives, and the SSM controls the final shape not to deviate from the allowable shape domain. We also employed the marker-based watershed technique to improve the results in low contrast regions. Moreover, the dynamic multi-atlas approach copes with the variations of the shape of the organ. Our results relate to two public datasets. Some researchers used nonpublic images (e.g. Refs. 11 and 18) and others utilized the PROMISE-12 dataset. Some methods used user-interaction (e.g. Refs. 10 and 19), while our algorithm is automatic and does not need a professional’s help. The PROMISE-12 contains simpler cases; therefore, the corresponding Dice metrics are better than the NCI-ISBI-2013 (e.g. Refs. 13 and 14). When we included PROMISE-12 in our available dataset, our results improved from 0.82 to 0.83.

Table 3. Evaluation of the output of the proposed method in different stages. DMA: Dynamic multi-atlas, DMA + Watershed: Refinement by the watershed technique, DMA + Watershed + SSM: Final improvement by the SSM.

Measure	DMA	DMA + Watershed	DMA + Watershed + SSM
Mean DSC	0.81 ± 0.05	0.82 ± 0.05	0.83 ± 0.05
Mean Jaccard	0.67 ± 0.07	0.69 ± 0.07	0.72 ± 0.06
Mean ACC	0.89 ± 0.02	0.90 ± 0.04	0.90 ± 0.03
Mean Error_Rate	0.10 ± 0.02	0.10 ± 0.04	0.09 ± 0.03

Table 4. A quantitative comparison between the proposed method and recent researches is shown.

Research	Method	Accessibility of the dataset	Dice index
Nelson <i>et al.</i> ¹²	Automatic atlas-based segmentation	NCI-ISBI-2013	0.79
RUNMC ¹⁰	Interactive prostate segmentation	NCI-ISBI-2013	0.808
Rusu <i>et al.</i> ¹⁰	Atlas-based	NCI-ISBI-2013	0.82
Mesadi <i>et al.</i> ²⁴	Shape and appearance model	NCI-ISBI-2013	0.83 (in central gland)
Guo <i>et al.</i> ¹¹	Deep learning + MAS + deformable models	Nonpublic	0.871 ± 0.004
Karimi <i>et al.</i> ¹³	Deep learning + SSM	PROMISE-12	0.88
Zhang <i>et al.</i> ¹⁴	Deep learning	PROMISE-12	0.905
Zhu <i>et al.</i> ¹⁸	Deep learning	Nonpublic	0.927
Bredell <i>et al.</i> ¹⁹	Deep learning	NCI-ISBI-2013	AutoCNN: 0.84
	Deep learning + user interaction	NCI-ISBI-2013	InterCNN: 0.97
Our Method	Deep learning + Multi-atlas + Watershed + SSM	NCI-ISBI-2013 PROMISE-12	0.83

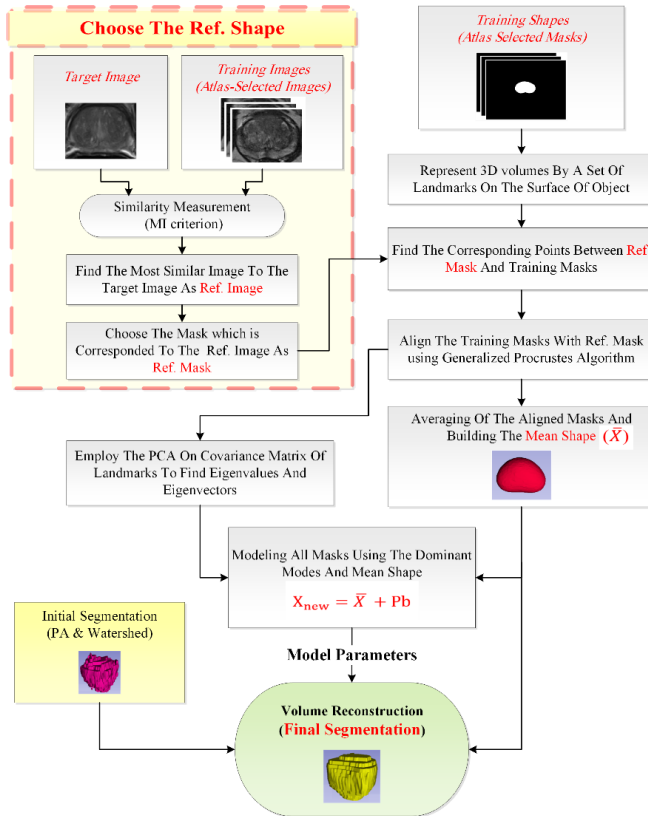


Fig. 7. Schematic diagram of the SSM model.

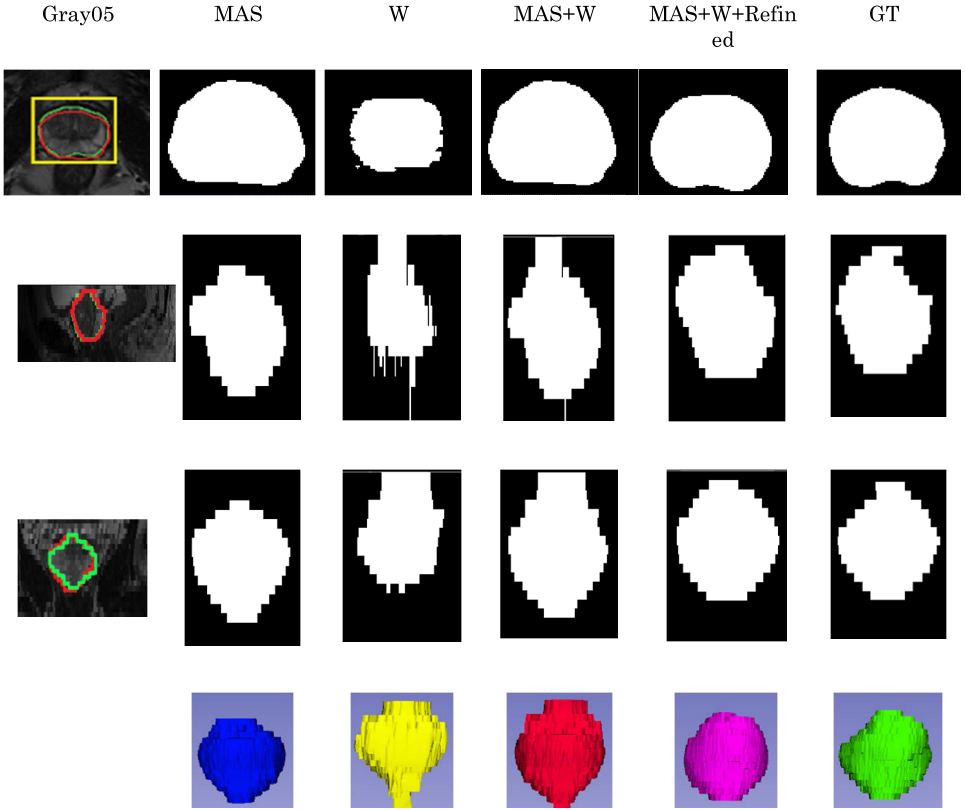


Fig. 8. (Color online) Segmentation results of Case #05 are shown. The first, second, and third rows represent the gray images and 2D/3D results in different steps of our method in axial, sagittal, and coronal views, respectively. The green contour is the ground-truth, while the blue, yellow, red, and magenta contours are the outcomes of the MAS, watershed, watershed + MAS, and final refinement, respectively. The yellow square in the axial view indicates the prostate’s ROI by the deep learning step.

The proposed method’s outcome is comparable to recent researches considering all the above points.

The convolutional neural network in Ref. 19 gets better results than ours; however, it is interactive and needs a professional user. Our method is automatic with no user interaction. Prostate’s segmentation is difficult compared to other tissues and requires an experienced physician’s supervision who is not accessible anywhere.

4.3. Qualitative evaluation

For better evaluation, we overlaid the axial, sagittal, and coronal views of the automatic (red contour) and gold standard (green contour) masks for typical cases (Fig. 8). The yellow square declares the prostate ROI obtained by the DNN stage. Figure 8 shows the effects of watershed and SSM algorithms on MAS results. It reveals that the watershed algorithm enhanced the results, especially in the apex and

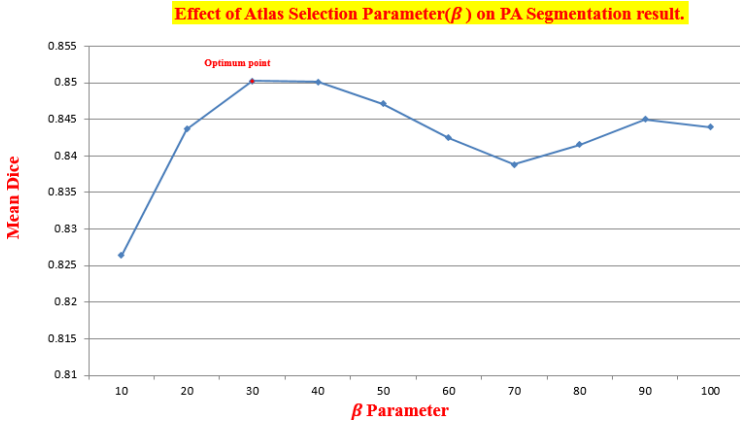


Fig. 9. The plot shows variations of the mean Dice index concerning β .

the base regions. Furthermore, the last row of Fig. 8 gives the surface rendering of different steps in our method.

4.4. MAS optimization

If the training images are similar to the target input, significant improvements will result in multi-atlas segmentation. We employed the MI similarity index as a measure to decide on similar images as shown in the following equation:

$$\frac{\text{MI}(C, A_i)}{\max \text{MI}(C, A_i)} > \beta. \tag{1}$$

In Eq. (1), the test image is C , the i th training image registered to the target is A_i and β is a threshold. When all training images are included in the selection, then β is zero. If we choose the most similar training image, then β equals one. Figure 9 illustrates variations of the Dice index for β values in the range 0.1 to 1.0. Regarding Fig. 9, the optimum β value is 0.30.

We performed several experiments with different values for the parameters of our algorithm. The optimum value of a parameter achieves the highest Dice index of the output. A typical parameter selection graph is shown in Fig. 9.

We categorized our segmentation results in different Dice intervals (Table 5). The accuracy of 42% of the results is 0.85 to 0.91, and the Dice index of 87.5% of data is greater than 75%. Therefore, the outcomes of the proposed algorithm are significant for most of the input images.

Table 5. Assessment of the achieved Dice indices.

Dice coefficient (%)	70–75	75–80	80–85	85–91
Number of cases	3	4	7	10

Table 6. Quantitative evaluation of four typical cases, including weak and good results ($W =$ Watershed algorithm).

Case No.	Method		Dice values		Description
	MAS	W	MAS + W	MAS + W + SSM	
Case #05	0.81	0.69	0.83	0.9	The best result.
Case #17	0.83	0.83	0.86	0.87	Consisting of a large prostate size
Case #07	0.62	0.56	0.61	0.72	Consisting of a small prostate size
Case #22	0.86	0.73	0.81	0.7	The worst obtained result

Table 6 represents four typical results. They include prostates of various shapes and sizes. Case-05 is a normal one. As shown in Table 6, the SSM reconstruction step improves the segmentation result significantly. The prostate is large in Case #17; however, our algorithm performed well. Our method’s performance is not acceptable for Case #07, which has a small organ. We predict to enhance the performance of our algorithm by enriching the dataset with diverse shapes and sizes. Our algorithm performs well in the MAS and MAS + W stages for Case #22.

5. Conclusion

In this paper, we proposed used deep neural networks, multi-atlas technique, watershed, and SSM-based reconstruction to segment the prostate in MR images. DNN defines the prostate’s ROI and removes the most irrelevant pixels. It enhances the registration accuracy and decreases the run-time of the code. The dynamic probabilistic atlas obtained more precise initial segmentation, and the watershed algorithm improved the result in the base and apex regions. We refined the acquired results by a dynamic SSM approach. Our method is regarded as an adaptive technique since it builds an atlas for each input image individually. In the future, we will upgrade our method in the base and apex regions more. Furthermore, we will employ more datasets and promote our results in the initial segmentation and image reconstruction stages.

References

1. P. A. Humphrey, *Prostate Pathology* (American Society for Clinical Pathology, Chicago, 2003).
2. J. Ferlay, M. Colombet, I. Soerjomataram, C. Mathers, D. M. Parkin, M. Piñeros, A. Znaor and F. Bray, “Estimating the global cancer incidence and mortality in 2018: GLOBOCAN sources and methods,” *Int. J. Cancer* **144**(8), 1941–1953 (2019).
3. F. H. Martini, *Fundamentals of Anatomy & Physiology*, 7th edn. (Pearson Education, 2006).
4. U. L. Stephansen, “Level-set appearance modeling for segmentation of anatomical structures in 3-d medical images,” Aalborg University (2012), pp. 5–13.
5. D. P. Huyskens, P. Maingon, L. Vanuytsel, V. Remouchamps, T. Roques, B. Dubray, B. Haas, P. Kunz, T. Coradi, R. Bühlman and R. Reddick, “A qualitative and a quantitative

- analysis of an auto-segmentation module for prostate cancer,” *Radiother. Oncol.* **90**(3), 337–345 (2009).
6. C. G. Roehrborn, P. Boyle, D. Bergner, T. Gray, M. Gittelman, T. Shown, A. Melman, R. B. Bracken, R. D. White, A. Taylor and D. Wang, “Serum prostate-specific antigen and prostate volume predict long-term changes in symptoms and flow rate: Results of a four-year, randomized trial comparing finasteride versus placebo,” *Urology* **54**(4), 662–669 (1999).
 7. G. Litjens, R. Toth, W. van de Ven, C. Hoeks, S. Kerkstra, B. van Ginneken, G. Vincent, G. Guillard, N. Birbeck, J. Zhang and R. Strand, “Evaluation of prostate segmentation algorithms for MRI: The PROMISE12 challenge,” *Med. Image Anal.* **18**(2), 359–373 (2014).
 8. S. Ghose, J. Mitra, A. Oliver, R. Marti, X. Lladó, J. Freixenet, J. C. Vilanova, D. Sidibé and F. Meriaudeau, “A random forest based classification approach to prostate segmentation in MRI,” in *MICCAI Grand Challenge: Prostate MR Image Segmentation* (Nice, France, 2012), pp. 125–128.
 9. S. Ghose, A. Oliver, R. Martí, X. Lladó, J. C. Vilanova, J. Freixenet, J. Mitra, D. Sidibé and F. Meriaudeau, “A survey of prostate segmentation methodologies in ultrasound, magnetic resonance and computed tomography images,” *Comput. Methods Programs Biomed.* **108**(1), 262–287 (2012).
 10. N. Bloch, A. Madabhushi, H. Huisman, J. Freymann, J. Kirby, M. Grauer, A. Enquobahrie, C. Jaffe, L. Clarke and K. Farahani, NCI-ISBI 2013 challenge: Automated segmentation of prostate structures. *The Cancer Imaging Archive*, 2015. Available at <https://wiki.cancerimagingarchive.net/display/Public/NCI-ISBI+2013+Challenge+-+Automated+Segmentation+of+Prostate+Structures> (accessed on 12 July 2021).
 11. Y. Guo, Y. Gao and D. Shen, “Deformable MR prostate segmentation via deep feature learning and sparse patch matching,” *IEEE Trans. Med. Imaging* **35**(4), 1077–1089 (2015).
 12. A. S. Nelson, J. Brockway, M. Lu, A. Javorek, S. Pirozzi and J. W. Piper, “Evaluation of an atlas-based segmentation method for prostate MRI,” *Int. J. Radiat. Oncol. Biol. Phys.* **90**(1), S419–S420 (2014).
 13. D. Karimi, G. Samei, C. Kesch, G. Nir and S. E. Salcudean, “Prostate segmentation in MRI using a convolutional neural network architecture and training strategy based on statistical shape models,” *Int. J. Comput. Assist. Radiol. Surg.* **13**(8), 1211–1219 (2018).
 14. Y. Zhang, J. Wu, W. Chen, Y. Chen and X. Tang, Prostate Segmentation Using Z-NET, arXiv:1901.06115v1.
 15. N. Aldoj, F. Biavati, M. Rutz, F. Michallek, S. Stober and M. Dewey, “Automatic prostate and prostate zones segmentation of magnetic resonance images using convolutional neural networks,” *Sci. Rep.* **10**, 14315 (2019).
 16. L. Yu, X. Yang, H. Chen, J. Qin and P. A. Heng, “Volumetric ConvNets with mixed residual connections for automated prostate segmentation from 3d mr images,” *31st AAAI Conf. Artificial Intelligence* (San Francisco, California, USA, 2007), pp. 66–72.
 17. R. Cheng, R. H. Roth, N. S. Lay, L. Lu, B. Turkbey, W. Gandler, E. S. McCreedy, T. J. Pohida, P. A. Pinto, P. L. Choyke and M. J. McAuliffe, “Automatic magnetic resonance prostate segmentation by deep learning with holistically nested networks,” *J. Med. Imaging* **4**(4), 041302 (2017).
 18. Y. Zhu, R. Wei, G. Gao, L. Ding, X. Zhang, X. Wang and J. Zhang, “Fully automatic segmentation on prostate MR images based on cascaded fully convolution network,” *J. Magn. Reson. Imaging* **49**(4), 1149–1156 (2019).

19. G. Bredell, C. Tanner and E. Konukoglu, "Iterative interaction training for segmentation editing networks," in *Int. Workshop Machine Learning in Medical Imaging* (Springer, Cham, 2018).
20. G. Vincent, G. Guillard and M. Bowes, "Fully automatic segmentation of the prostate using active appearance models," in *MICCAI Grand Challenge: Prostate MR Image Segmentation*, Vol. 2012 (2012) (Manchester 2012).
21. M. Kirschner, F. Jung and S. Wesarg, "Automatic prostate segmentation in MR images with a probabilistic active shape model," in *MICCAI Grand Challenge: Prostate MR Image Segmentation* (2012).
22. B. Maan and F. van der Heijden, "Prostate MR image segmentation using 3D active appearance models," in *MICCAI Grand Challenge: Prostate MR Image Segmentation* (2012).
23. T. F. Cootes, G. J. Edwards and C. J. Taylor, "Active appearance models," in *Euro Conf. Computer Vision* (Springer, Berlin, Heidelberg, 1998).
24. F. Mesadi, M. Cetin and T. Tasdizen, "Disjunctive normal shape and appearance priors with applications to image segmentation," in *Int. Conf. Medical Image Computing and Computer-Assisted Intervention* (Springer, Cham, 2015).
25. N. Makni, P. Puech, R. Lopes, A. S. Dewalle, O. Colot and N. Betrouni, "Combining a deformable model and a probabilistic framework for an automatic 3D segmentation of prostate on MRI," *Int. J. Comput. Assist. Radiol. Surg.* **4**(2), 181 (2009).
26. G. Litjens, N. Karssemeijer and H. Huisman, "A multi-atlas approach for prostate segmentation in MR images," *MICCAI Grand Challenge: Prostate MR Image Segmentation* 2012, (2012).
27. D. Stojanov and S. Koceski, "Topological MRI prostate segmentation method," in *2014 Federated Conf. Computer Science and Information Systems* (IEEE, 2014).
28. H. Moradi, A. H. Foruzan and Y. W. Chen, "Automatic segmentation of prostate in MR images using deep learning and multi-atlas techniques," in *2018 25th National and 3rd Int. Iranian Conf. Biomedical Engineering (ICBME)* (2018), pp. 1–4.
29. Livestrong (2003), <https://www.livestrong.com/article/339359-normal-prostate-weight>.
30. C. Dong, Y. W. Chen, A. H. Foruzan, L. Lin, X. H. Han, T. Tateyama, X. Wu, G. Xu and H. Jiang, "Segmentation of liver and spleen based on computational anatomy models," *Comput. Biol. Med.* **67**, 146–160 (2015).
31. M. Delavari, A. H. Foruzan and Y. W. Chen, "Accurate point correspondences using a modified coherent point drift algorithm," *Biomed. Signal Process. Control* **52**, 429–444 (2019).



Hamid Moradi received his B.S. degree from the Ashter University of Technology, Iran, and his M.S. degree from the Shahed University, Iran, in 2015. He is an expert in Intelligent Transportation Systems and electronic designing. From 2015 up to now, he has joined the electronic industry. His current research is in the field of medical image processing.



Amir Hossein Foruzan received his B.S. degree in Electrical Engineering from the Sharif University of Technology, Iran, his M.S., and Ph.D. degrees from Tehran University, Iran. He joined Shahed University in August 2011. From November 2008 up to now, he has collaborated with “Intelligent Image Processing Lab”, the Ritsumeikan University, Japan, and has visited there several times as a sabbatical. His research interests are medical image processing and applications of image processing in industrial fields.